Vallejo-Castro, L.; Mora Almerich, J.; Ortega Tamarit, B. (2022). Harmonic and Intermodulation Distortion Analysis in Directly Modulated Lasers Over Local and Remote Photonically Generated Millimeter-Wave Signals. Journal of Lightwave Technology. 40(15):5128-5140. https://doi.org/10.1109/JLT.2022.3172771

Harmonic and Intermodulation Distortion Analysis in Directly Modulated Lasers over Local and Remote Photonically Generated Millimeter-Wave Signals

Luis Vallejo, *Member, IEEE*, José Mora, and Beatriz Ortega, *Senior Member, IEEE*

***Abstract*—This paper presents a comprehensive analytical derivation and experimental evaluation of the impact of harmonic and intermodulation distortion on data transmission over local and remote photonically generated millimeter wave (mmW) signals over an optical fronthaul based on a directly modulated laser (DML) and carrier-suppressed (CS) external modulation for frequency up-conversion. Frequency response of different harmonic distortion (HD) and intermodulation (IMD) terms are measured for a 40 GHz signal under back-to-back, local and remote scenarios for the sake of comparison.**

Furthermore, measurements of error vector magnitude (EVM) of single and multiband QPSK signals are presented in good agreement with the frequency measurements for $(2\omega_k)$, $(\omega_k - \omega_l)$ and $(\omega_k + \omega_l)$-type distortion terms. Wideband signals with in-band distortion and multiband signals with out-of-band distortion are examples that need to be transmitted over local generation mmW approach in cloud-radio access networks (C-RAN), in spite of the high performance achieved by remote generation approach due to the combined effect of fiber dispersion and laser chirp. Results will serve as valuable guidelines for 6G networks deployment in concrete application scenarios.

***Index Terms*—Cloud radio access networks, millimeter wave, optical access networks, intermodulation.**

I. Introduction

THE continuous proliferation of rich-video applications, interactive services, mobile cloud services or machine-to-machine (M2M) communications leads to an explosive increase of the global mobile traffic, which was estimated as 62 EB and 5016 EB per month in 2020 and 2030, respectively [1]. The main reasons for such explosive growth are the total number of mobile broadband subscribers worldwide which will reach 17.1 billion with an average data consumption over 250 GB per month and also, the number of M2M subscriptions which are expected to be around 97 billion by 2030.

Future mobile communications, i.e. sixth generation (6G) networks, will support novel scenarios such as holographic-type communications, extended reality, ubiquitous intelligence, tactile internet, multi-sense experience and digital twin amongst others. Accordingly, the technical requirements for 6G are significantly more stringent than those in fifth generation (5G) networks, and include minimal latency of 0.1 ms, user experience of 1 Gb/s and peaks rate of 1 Tb/s. Therefore, advanced enabling technologies will be required to provide new spectrum, virtual infrastructures, air interfaces, architectures and paradigms in 6G networks [2]. The millimeter wave (mmW) technology, already introduced by the 5G new radio, is still essential in 6G networks due to the huge bandwidth, small antenna size and larger arrays with narrow beams. Analog-radio-over-fiber (A-RoF) solutions provide cost-efficient, low latency and large bandwidth links in cloud-radio access networks (C-RAN) where the availability and costs of the optical infrastructure become critical, especially due to small-cell environment [3, 4, 5, 6].

Fig. 1(a) illustrates a C-RAN providing indoor and outdoor mmW small cells access as well as fiber broadband access in residential areas. The network architecture hosts the baseband units (BBUs) at the central office (CO) separated from the remote radio heads (RRH) or optical network units (ONU). BBUs at CO host medium access control (MAC) layer functions, digital-to-analog and analog-to-digital conversion (DAC/ADC), radio frequency (RF) frontends and baseband processing [7]. Therefore, simplified RRHs only provide opto-electronic conversion and further amplification. Broad coverage can be provided due to a large number of remote RRHs connected to a centralized BBU pool with a span fiber link, typically up to 10 km for 5G.

Moreover, the literature presents a large number of approaches for photonic generation of mmW signals using electronics components with reduced bandwidth while offering low phase noise and frequency tunability [8]. Optical frequency multiplication by using an external lithium niobate Mach-Zehnder modulator (MZM) biased at carrier suppression (CS) point is one of the most attractive options due to easy implementation, high quality and efficient mmW signal generation [9].

In the A-RoF scheme, mmW signals can be transmitted either using an intermediate frequency (IF) or radiofrequency (RF) over optical fiber. In the former technique, which corresponds to a local generation approach, the mmW up-conversion is held at the remote radio head (RRH) in the C-RAN just before wireless transmission (Fig. 1(b)). However, in the latter one, i.e. remote generation approach, the central office (CO) transmits the mmW signal modulated into the optical domain over fiber fronthaul network to the RRH without the need for frequency up-conversion at the RRH side (Fig. 1(c)). In spite of the complexity and costs of RRHs due to the need for mmW local oscillator and high speed mixers in the

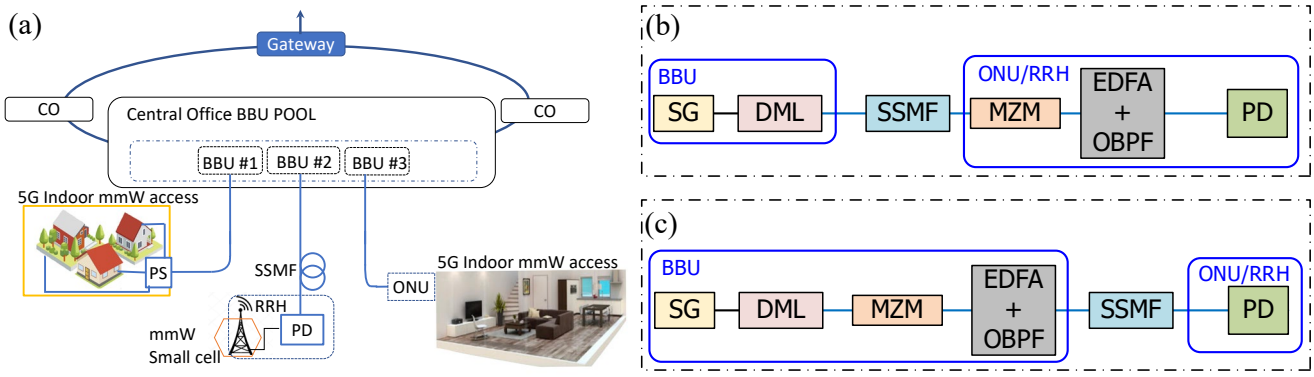

Fig. 1. (a) C-RAN architecture. Schematics for (b) local and (c) remote configuration. CO: central office, ONU: optical network unit, RRH: radio remote head, BBU: baseband unit, PS: power splitter, SSMF: standard single mode fiber, PD: photodetector, SG: signal generator, DML: directly modulated laser, MZM: Mach-Zehnder modulator, EDFA: erbium doped amplifier, OBPF: optical band pass filter.

local approach, this is an attractive solution due to its reduced impact of fiber chromatic dispersion [10]. Moreover, the use of photonic signal generation techniques allows to employ lower speed optoelectronic devices.

However, recent work demonstrated that the combined effect of dispersion and laser chirp in the remote approach leads to higher frequency response in the photonically generated mmW band [11], oppositely to the system frequency response in baseband, which is very promising for deployment of future C-RANs. Moreover, it is well known that optical nonlinearities limit the overall system performance and different techniques have been proposed to overcome intermodulation distortions (IMD), such as optical feedforward, predistortion or filtering IMD tones [12]. Several papers in the literature analyze the impact of the IMD in RoF signals due to the nonlinear MZM response [13] and also the laser chirp, fiber transmission and photodetection in mmW signals [14]. However, further work is required on the impact of harmonic distortion (HD) and IMD in data transmission over photonically generated mmW signals in order to assess the network performance under specific scenarios.

In this work, we evaluate the impact of harmonic and intermodulation distortion in data transmission over local and remote photonically generated 40 GHz signal over an optical fronthaul based on a DML and CS external modulation for frequency up-conversion. For the first time to the authors´ knowledge, a comprehensive analytical derivation and experimental evaluation of the HD and IMD frequency response of both approaches is provided to identify the optimal setup for concrete application scenarios in 6G networks.

The paper is structured as follows. Section II presents the analytical formulation of the second-order HD and IMD terms in local and remote approaches and experimental measurements of their frequency response. Section III shows the measurement results of the system output electrical spectra, and performance for a single band QPSK signal of different bandwidths over 40 GHz and several multiband signals under remote and local approaches in 10 km fiber links, in order to evaluate the impact of nonlinear distortions in photonically generated mmW signals. Finally, Section IV summarizes the main conclusions of this work.

II. Analysis of HD and IMD in DML Signal Transmission over Photonically Generated MMW Signals

In this section, we evaluate local and remote architectures for photonic mmW signal generation in terms of nonlinearities. Fig. 1(b) and (c) show a DML located at the BBU, emitting an optical carrier with angular frequency ω_0 which is data modulated in both schematics.

In the local configuration depicted in Fig. 1(b), the optical signal emitted by the DML is launched into the standard single mode fiber (SSMF) and then, it is up-converted by a single tone with an angular modulation frecuency given by $\omega_{RF} = 2\pi f_{RF}$ in the MZM, which is biased at null point for CS modulation before opto-electronic conversion at the photodiode in the ONU/RRH. However, in the remote configuration scheme depicted in Fig. 1(c), the DML output signal is launched into the CS-MZM to be modulated by ω_{RF} tone signal and then, the resulting signal is transmitted through a SSMF link. Both configurations lead to different system response due to fiber dispersion impact on the transmitted signal [11].

In the following, an analytical study of the nonlinear frequency response of both approaches is presented. Let us consider the output electric field of a laser emitting at ω_0, which is directly modulated by a single tone at angular modulation frequency of $\omega = 2\pi f$, given by [15]:

$$E_{DML}(t) = \sqrt{P_o(1 + m_{AM} \cdot cos\ \omega t)}e^{jm_{PM} \cdot cos(\omega t + \Delta\varphi)}e^{j\omega_0 t} \quad (1)$$

where P_o is the laser output power, m_{AM} and m_{PM} are the amplitude and phase modulation indexes, respectively, and $\Delta\varphi$ is the phase difference between both modulations. These terms are related to the chirp characteristics of the laser, i.e. linewidth enhancement factor, α, and adiabatic laser chirp, κ, as follows [15]:

$$\frac{m_{PM}}{m_{AM}} \cdot e^{j\Delta\varphi} = \alpha\left(1 - j\frac{\kappa P_o}{\omega}\right) \quad (2)$$

The linear time response of the DML is given by:

$$h_{DML}(t) = m_o + m_+(\omega) \cdot e^{j\omega t} + m_-(\omega) \cdot e^{-j\omega t} \quad (3)$$

where the m_+ and m_- index modulations can be expressed in terms of amplitude, m_{AM}, and phase, m_{PM}, modulation indexes:

$$m_+(\omega) = \frac{1}{2}\left(m_{AM} + jm_{PM}e^{j\Delta\varphi}\right)$$
$$m_-(\omega) = \frac{1}{2}\left(m_{AM} + jm_{PM}e^{-j\Delta\varphi}\right) \quad (4)$$

In this paper, we consider multiband signal transmission, i.e., the laser is directly modulated by k-tones with angular modulation frequencies $\omega_k = 2\pi f_k$, which leads to the following time response due to DML nonlinear behavior [16, 17]:

$$\begin{aligned} h_{DML}(t) &= m_o \\ &+ \sum_k m_+(\omega_k)\cdot e^{j\omega_k t} + m_-(\omega_k)\cdot e^{-j\omega_k t} \\ &+ \sum_k m_+(2\omega_k)\cdot e^{j2\omega_k t} + m_-(2\omega_k)\cdot e^{-j2\omega_k t} \\ &+ \sum_k\sum_{l\neq k} m_+(\omega_k - \omega_l)\cdot e^{j(\omega_k-\omega_l)t} + m_-(\omega_k - \omega_l)\cdot e^{-j(\omega_k-\omega_l)t} \\ &+ \sum_k\sum_{l\neq k} m_+(\omega_k + \omega_l)\cdot e^{j(\omega_k+\omega_l)t} + m_-(\omega_k + \omega_l)\cdot e^{-j(\omega_k+\omega_l)t} \end{aligned} \quad (5)$$

where $m_\pm(2\omega_k)$ accounts for the second-order harmonic distortion and $m_\pm(\omega_k \pm \omega_l)$ corresponds to the second-order intermodulation products of the DML. All these terms $m_\pm(\omega)$ can be obtained from solving the dynamic equations of the DML under large-signal regime. Since this evaluation is far from the scope of this manuscript, we present a theoretical analysis which permits to obtain the response of the proposed structures from the DML response.

The time response of the MZM driven by a single tone at RF, $\omega_{RF} = 2\pi f_{RF}$, under CS bias point, is given by:

$$\begin{aligned} h_{MZM}(t) = m_{RF} &\cdot \left[A_+(\omega_{RF})e^{j\omega_{RF}t}\right. \\ &\left. + A_-(\omega_{RF})e^{-j\omega_{RF}t}\right] \end{aligned} \quad (6)$$

where $A_\pm(\omega_{RF})$ are the MZM amplitude coefficients and m_{RF} is the modulation RF index.

Additionally, the time response of the signal propagation in SSMF fiber, $h_{SSMF}(t)$, can be expressed as [18]:

$$h_{SSMF}(t) = \frac{1}{\sqrt{j2\pi\beta_2 L}} e^{j\frac{\pi}{2\beta_2 L}t^2} \quad (7)$$

where L is the fiber length and the dispersion parameter, β_2, is the second derivative of the propagation constant with respect to the optical angular frequency at ω_0.

According to the analytical formulation provided in [11], Table I shows how to calculate the optical field at the input of the photodiode, $E(t)$, for optical back to back (OB2B), local and remote configurations (see Fig. 1).

TABLE I. ANALYTICAL EXPRESSION OF THE OPTICAL FIELD AT THE INPUT OF THE PHOTODIODE.

Configuration	$E(t)$	
OB2B	$E_{B2B}(t) = E_{DML}(t)\cdot h_{MZM}(t)$	(8)
LOCAL	$E_{LC}(t) = [E_{DML}(t) \otimes h_{SSMF}(t)]\cdot h_{MZM}(t)$	(9)
REMOTE	$E_{RC}(t) = [E_{DML}(t)\cdot h_{MZM}(t)] \otimes h_{SSMF}(t)$	(10)

Then, the electrical current obtained at the photodiode, $i(t)$, can be calculated as:

$$i(t) = \Re \cdot P(t) = \Re \cdot |E(t)|^2 \quad (11)$$

where $\Re$ is the photodiode responsivity and $P(t)$ is the detected optical power. Accordingly, the electrical voltage is given by:

$$V_{RF}(t) = Z_\Omega \cdot i(t) \quad (12)$$

where Z_Ω is the total impedance of the optical receiver.

After photodetection, the most significant distortion terms correspond to the HD at the frequency $2\omega_k$ and the IMD at $\omega_k \pm \omega_l$ in the mmW band of interest (i.e. $2\omega_{RF}$). While the evaluation of $V_{RF}(2\omega_{RF} \pm \omega_k)$ provides the amplitude response of the transmission system operating in the mmW band, the evaluation of V_{RF} at other frequency values such as $V_{RF}(2\omega_{RF} \pm 2\omega_k)$ and $V_{RF}(2\omega_{RF} \pm \omega_k \pm \omega_l)$ allows us to obtain nonlinear HD and IMD response, respectively; and therefore, to evaluate the impact on the data transmission.

Tables II, III and IV show the analytical response for $(2\omega_k)$, $(\omega_k - \omega_l)$ and $(\omega_k + \omega_l)$-type terms, respectively, for OB2B, local and remote configurations in the mmW band. Note that all of them are equivalent when the dispersive effects are negligible, i.e., the product $\beta_2 L$ tends to zero. HD an IMD contribution for local and remote schemes are determined by the dispersion at the IF frequency (ω) or the RF frequency (ω_{RF}), respectively. Indeed, the terms $m_\pm(2\omega_k)$ and $m_\pm(\omega_k \pm \omega_l)$ are determined mainly by the phase factors proportional to $\beta_2 L\omega^2$ or $\beta_2 L\omega_{RF}\omega^2$ for local and remote, respectively, compared to OB2B scenario. Because of design properties, the RF frequency ω_{RF} is higher than ω, so the different response under remote scheme in comparison with local scheme, i.e. $\beta_2 L\omega^2$ is less relevant for lower frequencies and therefore, similar to OB2B response. Moreover, the DML chirp is present as $m_\pm(\omega_k)$ terms, which combines with dispersion leading to an impact on the corresponding HD and IMD contributions

For the sake of validation and better understanding of the nonlinear system behavior, these terms are also measured in our experimental setup, which employs a DML (Optical Zonu,

TABLE II. SECOND-ORDER HD ($2\omega_{RF} \pm 2\omega_k$) ANALYTICAL RESPONSE.

	$V_{RF}(2\omega_{RF} \pm 2\omega_k)$	
OB2B	$\left\|m_{RF}\right\|^2 A_+(\omega_{RF})A_-^*(\omega_{RF})\left[m_o m_\mp^*(2\omega_k) + m_o^* m_\pm(2\omega_k)\right]$	(13)
LOCAL	$\left\|m_{RF}\right\|^2 A_+(\omega_{RF})A_-^*(\omega_{RF})\left[m_o m_\mp^*(2\omega_k)\cdot e^{-j2\beta_2\beta_2 L\omega_k^2} + m_o^* m_\pm(2\omega_k)\cdot e^{j2\beta_2\beta_2 L\omega_k^2}\right]$	(14)
REMOTE	$\left\|m_{RF}\right\|^2 A_+(\omega_{RF})A_-^*(\omega_{RF})\left[m_o m_\mp^*(2\omega_k)\cdot e^{-j2\beta_2 L[\omega_k^2 \pm \omega_{RF}\omega_k]} + m_o^* m_\pm(2\omega_k)\cdot e^{j2\beta_2 L[\omega_k^2 \pm \omega_{RF}\omega_k]}\right]$	(15)

TABLE III. SECOND-ORDER IMD $(2\omega_{RF} \pm (\omega_k - \omega_l))$ ANALYTICAL RESPONSE.

	$V_{RF}(2\omega_{RF} \pm (\omega_k - \omega_l))$	
OB2B	$\left\|m_{RF}\right\|^2 A_+(\omega_{RF})A_-^*(\omega_{RF})\left[m_o m_{\mp}^*(\omega_k - \omega_l) + m_o^* m_{\pm}(\omega_k - \omega_l)\right]$	(16)
LOCAL	$\left\|m_{RF}\right\|^2 A_+(\omega_{RF})A_-^*(\omega_{RF})\left[m_o m_{\mp}^*(\omega_k - \omega_l)\cdot e^{-j\frac{1}{2}\beta_2 L(\omega_k-\omega_l)^2} + m_o^* m_{\pm}(\omega_k - \omega_l)\cdot e^{j\frac{1}{2}\beta_2 L(\omega_k-\omega_l)^2}\right]$	(17)
REMOTE	$\left\|m_{RF}\right\|^2 A_+(\omega_{RF})A_-^*(\omega_{RF})\left[m_o m_{\mp}^*(\omega_k - \omega_l)\cdot e^{-j\frac{1}{2}\beta_2 L[(\omega_k-\omega_l)^2 \pm \omega_{RF}(\omega_k-\omega_l)]} + m_o^* m_{\pm}(\omega_k - \omega_l)\cdot e^{j\frac{1}{2}\beta_2 L[(\omega_k-\omega_l)^2 \pm \omega_{RF}(\omega_k-\omega_l)]}\right]$	(18)

TABLE IV. SECOND-ORDER IMD $(2\omega_{RF} \pm (\omega_k + \omega_l))$ ANALYTICAL RESPONSE.

	$V_{RF}(2\omega_{RF} \pm (\omega_k + \omega_l))$	
OB2B	$m_{RF}^2 A_+(\omega_{RF})A_-^*(\omega_{RF})\left[m_o m_{\mp}^*(\omega_k + \omega_l) + m_o^* m_{\pm}(\omega_k + \omega_l)\right]$	(19)
LOCAL	$\left\|m_{RF}\right\|^2 A_+(\omega_{RF})A_-^*(\omega_{RF})\left[m_o m_{\mp}^*(\omega_k + \omega_l)\cdot e^{-j\frac{1}{2}\beta_2 L(\omega_k+\omega_l)^2} + m_o^* m_{\pm}(\omega_k - \omega_l)\cdot e^{j\frac{1}{2}\beta_2 L(\omega_k+\omega_l)^2}\right]$	(20)
REMOTE	$\left\|m_{RF}\right\|^2 A_+(\omega_{RF})A_-^*(\omega_{RF})\left[m_o m_{\mp}^*(\omega_k + \omega_l)\cdot e^{-j\frac{1}{2}\beta_2 L[(\omega_k+\omega_l)^2 \pm \omega_{RF}(\omega_k+\omega_l)]} + m_o^* m_{\pm}(\omega_k + \omega_l)\cdot e^{j\frac{1}{2}\beta_2 L[(\omega_k+\omega_l)^2 \pm \omega_{RF}(\omega_k+\omega_l)]}\right]$	(21)

OZ516) emitting an optical carrier centered at 1553.5 nm with 5.6 dBm optical power. The output signal from a vector signal generator (VSG) (Rohde & Schwarz, SMW200A) composed of one or multiple RF subcarriers is used to modulate the laser, the modulation frequency at the MZM is $f_{RF} = 20$ GHz and the fiber length is 10 Km ($\beta_2 = -22.1\,\mathrm{ps}^2/\mathrm{km}$). After photodetection, a signal analyzer (SA) (Rohde Schwarz, FSW43) displays all frequency components and nonlinear response can be separately measured.

Firstly, the electrical back-to-back (EB2B) measurement has been done for the sake of characterization of the electrical signal (f_1) applied to the DML where signal generator and analyser are directly connected. The EB2B measurement is included in Figs. 2, 3 and 4 where evaluation of $(2\omega_k)$, $(\omega_\mathbf{k} - \omega_\mathbf{l})$ and $(\omega_\mathbf{k} + \omega_\mathbf{l})$-type distortion terms are analysed, respectively.

With regards to the evaluation of $(2\omega_k)$-type term, the VSG is configured to generate an RF-tone centered at f_1 which is introduced in the DML and the RF power is measured at the frequency $2f_{RF} \pm 2f_1$ for B2B, local and remote configuration. For the sake of brevity, since lower and upper bands lead to similar results, Fig. 2 shows the amplitude response for different frequency values f_1 (x-axis) corresponding to the lower band. Firstly, we observe that OB2B amplitude response of Fig. 2 is directly proportional to the response of the DML as shown in Eq. (13). Indeed, we can identify the typical regimes of a DML corresponding to operation frequency close to the relaxation frequency or not [15]. According to [11], the amplitude response of the DML leads to a relaxation frequency

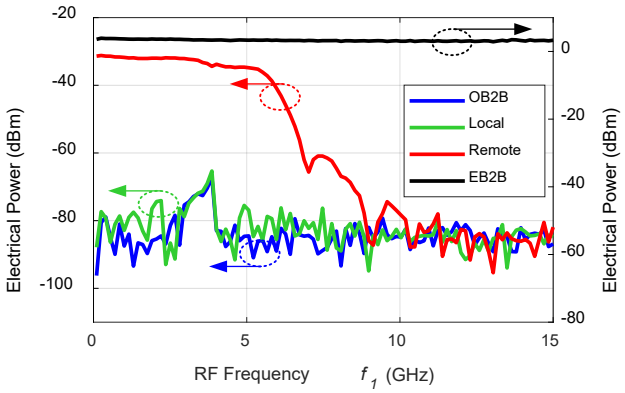

Fig. 3. Experimental second-order IMD $(2\omega_{RF} - (\omega_2 - \omega_1))$ for OB2B, local and remote configuration (left axis). EB2B signal measurement is included as a reference (right axis).

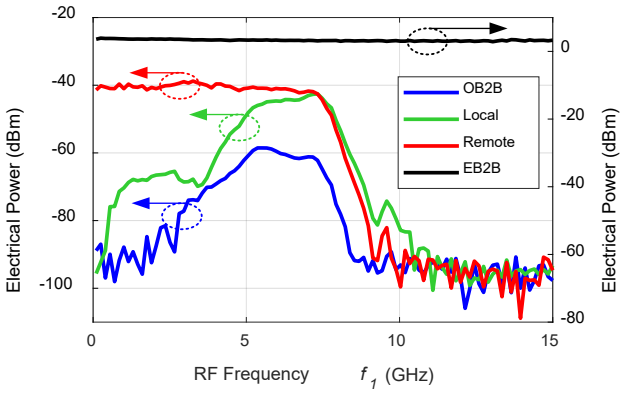

Fig. 2. Experimental second-order HD $(2\omega_{RF} - 2\omega_1)$ for OB2B, local and remote configuration (left axis). EB2B signal measurement is included as a reference (right axis).

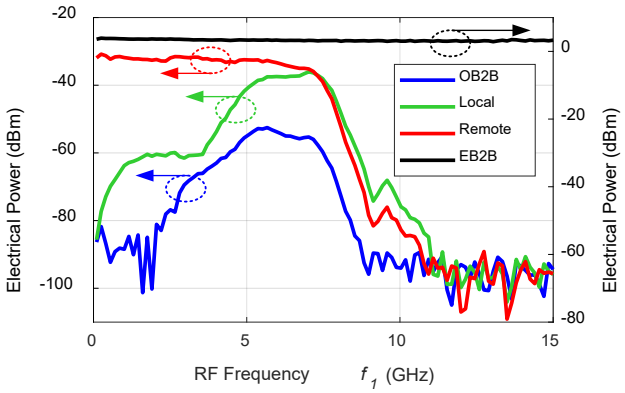

Fig. 4. Experimental second-order IMD $(2\omega_{RF} - (\omega_2 + \omega_1))$ for OB2B, local and remote configuration. EB2B signal measurement is included as a reference.

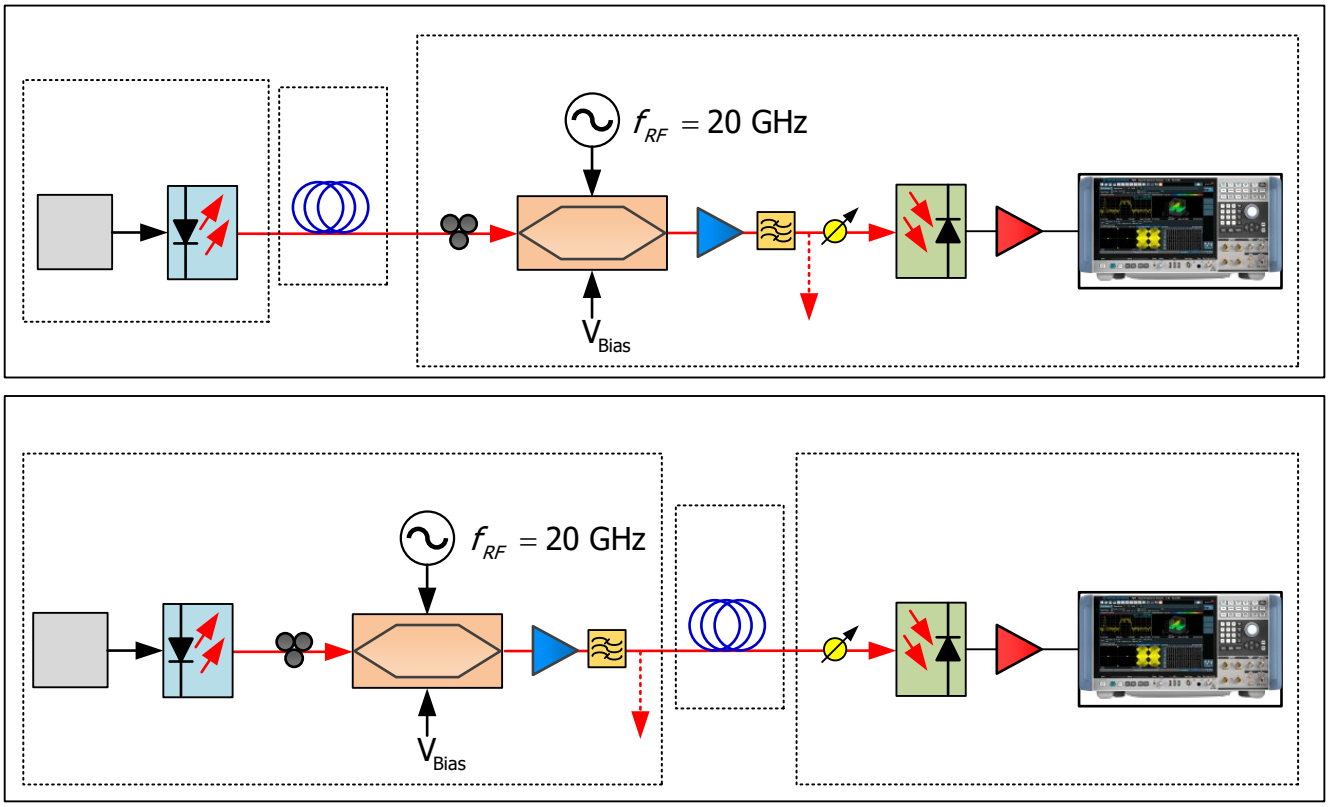

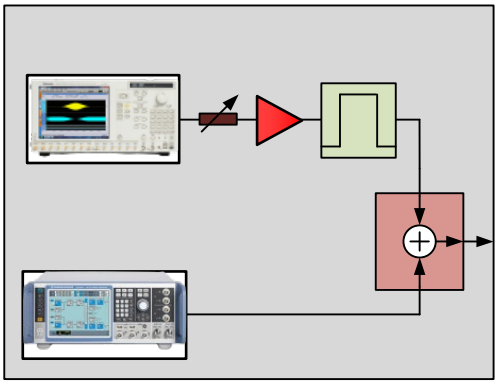

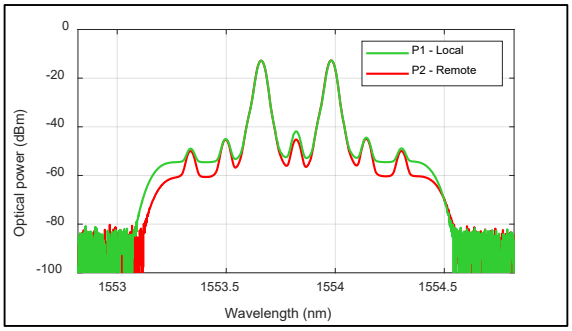

Fig. 5. (a) Local and (b) remote setups, (c) data generator scheme and (d) optical spectra for local (P1) and remote (P2) setups. CO: central office, BBU: baseband unit, DG: digital generator, DML: directly modulated laser, PC: polarization controller, MZM: Mach Zehnder modulator, SG: signal generator, EDFA: erbium doped amplifier, OBPF: optical band pass filter, ODN: optical distribution network, SSMF: standard single mode fiber, RRH: radio remote head, PD: photodetector, EA: electrical amplifier, SA: signal analyser, A: attenuator, EBPF: electrical band pass filter, EC: electrical combiner.

close to 6.5 GHz where the distortion is higher than in lower frequencies. Frequencies lower than 3.5 GHz lead to signal nonlinearities arising mainly from the power-current (P-I) curve and therefore, this low-frequency region is selected due to minimum distortion.

Additionally, Fig. 2 shows the amplitude response under local configuration for mmW signal generation, which resembles the DML output signal propagated along the same dispersive fiber link, as can be observed in Eq. (14). In this sense, maximum response of HD ($2\omega_{RF} - 2\omega_1$) is found in a 2.5 GHz wideband centered at 6.5 GHz in OB2B configuration, similar to local configuration, as expected from the slight contribution of the dispersion factor $e^{j2\beta_2 L\omega^2}$ in Eq. (14) while shows negligible HD at lower frequencies than 3.5 GHz. However, the evaluation of HD under remote configuration leads to a larger dispersion factor given by $e^{j2\beta_2 L\omega_{RF}\omega}$ as shown in Eq. (15), which leads to a significantly different frequency response. In this case, HD is held all over the frequency band and therefore, significant impact is expected even at low frequencies within the DML modulation band (-40 dBm electrical power). Note that differences between HD in local and remote configurations arise mainly from dispersion effects since the dependence on the laser chirp is identical in Eq. (14) and Eq. (15). Therefore, significant impact on the transmitted signals will be observed under remote configuration, especially when two bands are transmitted satisfying $\omega_2 = 2\omega_1$.

In the following, two RF tones, f_1 and f_2, are generated with constant frequency spacing of 100 MHz while both subcarriers are tuned simultaneously and the amplitude response is measured at the frequency $2f_{RF} - (f_2 - f_1)$ to

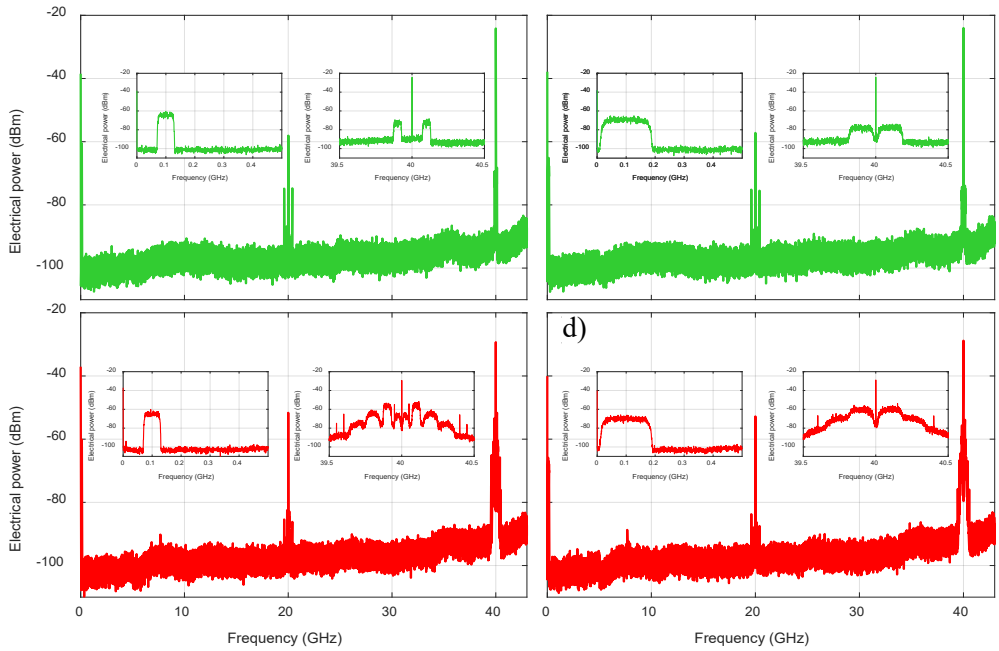

Fig. 6. Electrical spectra of transmitted signals with different bandwidths for local configuration: (a) 50 MHz, (b) 150 MHz; and remote configuration: (c) 50 MHz and (d) 150 MHz. Insets show the detail of the spectrum at baseband (left) and mmW band (right).

obtain the IMD $(2\omega_{RF} - (\omega_2 - \omega_1))$, as shown in Fig. 3. Table III shows the analytical expressions where it can be observed that local configuration leads to similar results than OB2B setup due to the small contribution of dispersion factor $\frac{1}{2}\beta_2 L(\omega_k - \omega_l)^2$ in Eq. (17) compared to the phase change $\frac{1}{2}\beta_2 L\omega_{RF}(\omega_k - \omega_l)$ introduced by remote configuration, as shown in Eq. (18). Note that OB2B and local configuration lead to the cancellation of electrical power at this IMD term IMD over the entire frequency range while the remote configuration leads to -30 dBm power at low frequencies. This IMD-term distortion will have significant impact when two signals transmitted with ω_1 and ω_2 satisfy $\omega_2 - \omega_1 = \omega_1$, so the first band ω_1 will directly notice the impact of this $(\omega_2 - \omega_1)$-type IMD term.

Finally, the impact of IMD $(2\omega_{RF} - (\omega_1 + \omega_2))$ term has been experimentally obtained by using two RF tones tuned simultaneously at f_1 and f_2 with a constant separation of 100 MHz and measuring the amplitude response at the frequency $2f_{RF} - (f_2 + f_1)$ (see Fig. 4). Note that in this case, when two signals with ω_1 and ω_2 are transmitted, a third band given by $\omega_3 = \omega_1 + \omega_2$ will notice the impact of this IMD-term distortion. Also, the equations of Table II and IV lead to similar results when ω_1 is close to ω_2. In this case, the amplitude response of HD $(2\omega_{RF} - 2\omega_1)$ and IMD $(2\omega_{RF} - (\omega_2 + \omega_1))$ are very similar for all scenarios, as theoretically expected.

Although remote setup leads to similar distortion level (-30 dBm in Fig. 4) than IMD $(2\omega_{RF} - (\omega_2 - \omega_1))$, the evaluation of this IMD term in the mmW band leads to slightly different results in this case compared to previous terms. In this case, OB2B and local configuration show significant values of distortion in the band centered at 6.5 GHz (-55dBm and -38 dBm, respectively) due to the intrinsic characteristic of the DML used experimentally.

III. EXPERIMENTAL TRANSMISSION RESULTS

A. Experimental setup

In this section we experimentally measured the impact of HD and IMD distortions on the signal transmission. Fig. 5 shows the experimental setups of local and remote mmW signal generation approaches. In this experiment, the DML, with an output power of 7dBm, is modulated by data signal which is generated by the data generator (DG) at central office (CO)-baseband unit (BBU). In the local generation scheme shown in Fig. 5(a), the optical signal emitted by the DML is

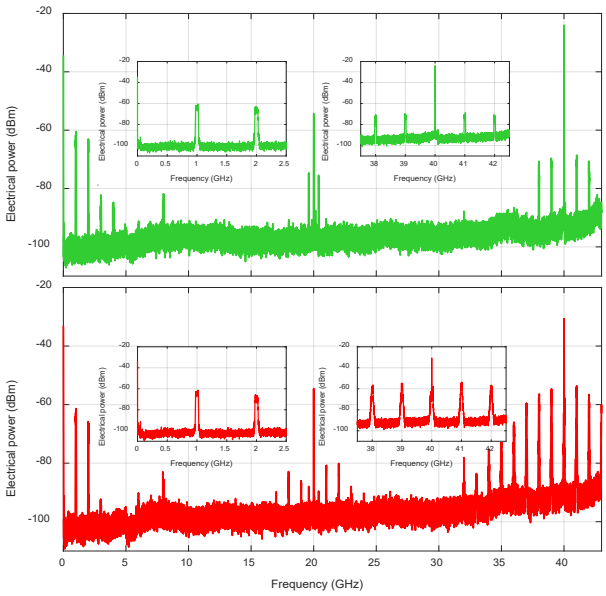

Fig. 7. Electrical spectra of dual band transmitted signals, centered at $f_1 = 1$ GHz and $f_2 = 2$ GHz: (a) local configuration and (b) remote configuration.

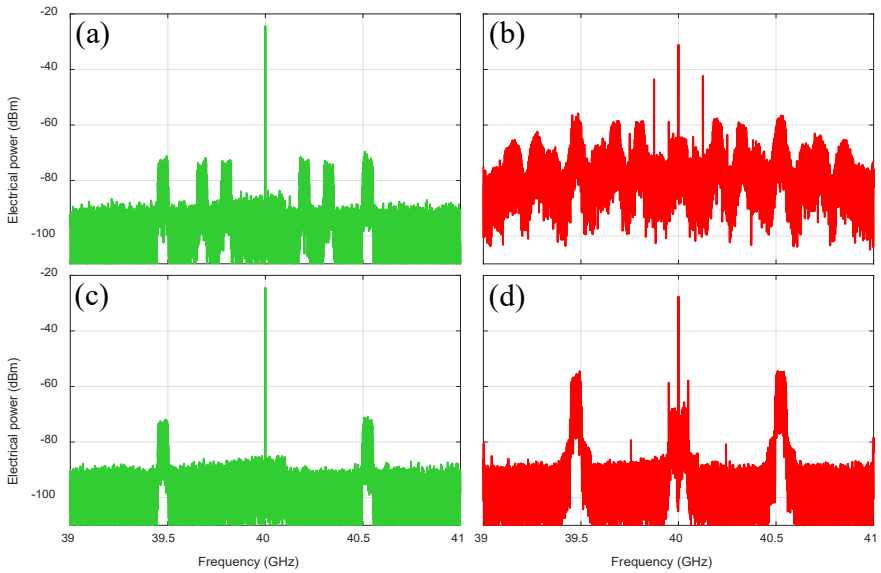

Fig. 8. Electrical spectra measurements after photodetection of three-band signal transmission under: (a) local scheme and (b) remote scheme. Measurements shown in (c) and (d) correspond to electrical spectra measurement when only one band is transmitted under local and remote schemes, respectively.

transmitted over the standard single mode fiber (SSMF) link and up converted just before the the opto-electronic conversion at the photodetector (PD). The polarization of the optical signal is tuned by a polarization controller (PC) and then launched into the Mach-Zehnder Modulator (MZM) (Sumitomo T.DEH1.5-40X-ADC-Y-Z), which is biased at the null transmission point (V_π), i.e. 7.84 V, to obtain the carrier suppressed optical signal. The MZM is driven with an electrical signal tone at 20 GHz and 23 dBm electrical power generated by a signal generator-3 (SG) (Agilent 8267C). Then, the optical signal is amplified by an erbium doped fiber amplifier (EDFA) (Amonics AEDFA-23-B-FA) with 20.1 dBm fixed output optical power and filtered out by an optical band pass filter (OBPF) (Alnair BVF-100) with bandwidth $\Delta\lambda$ = 1.25 nm in order to reduce the amplified spontaneous emission (ASE). Finally, a variable optical attenuator (VOA) allows to adjust the RoP (see Figs. 5(a) and (b)) just before the PD (Finisar XPDV3120R). It is working in linear regime to generate a mmW signal at desired frequency by beating of the sidebands. After photodetection, the 43 GHz bandwidth SA (FSW43) performs both electrical spectra measurements and signal demodulation. The quality of the recovered signals is provided in terms of error vector magnitude (EVM) and signal constellations

On the other hand, the remote configuration is shown in Fig. 5(b) where the up-conversion is held at CO-BBU using the CS-MZM and then the optical signal is transmitted along the 10 km SSMF link. The MZM is driven and biased in the same conditions as in the local scheme. The optical signal is amplified and filtered out by the EDFA and OBPF, respectively. Finally, the electrical signal is generated at the 40 GHz band at the PD.

The data generator scheme is shown in Fig. 5(c) where data band is generated, amplified and filtered out by the SG (i.e. Tektronix AWG7122C or Rohde & Schwarz SMW200A), electrical amplifier-1 (EA) (Communication Technologies SHF-810) and electrical band pass filter (EBPF) (Minicircuits 14780), respectively. Different bands can be generated from other SGs and combined by the electrical combiner (EC) (Minicircuits ZFRSC-42) in multiband scenarios.

The optical spectrum at the OBPF output, shown in Fig. 5(d), is measured by an optical spectrum analyser (OSA) (Yokogawa AQ6370C) at P1 and P2 points for local and remote

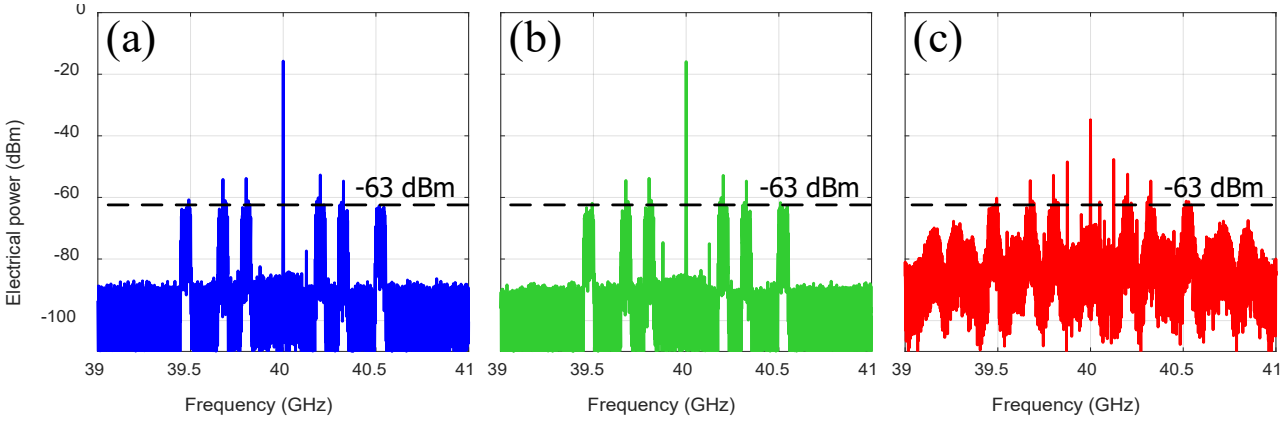

Fig. 9. Electrical spectra of three-band transmitted signal under: (a) OB2B, (b) local and (c) remote schemes for similar electrical power level.

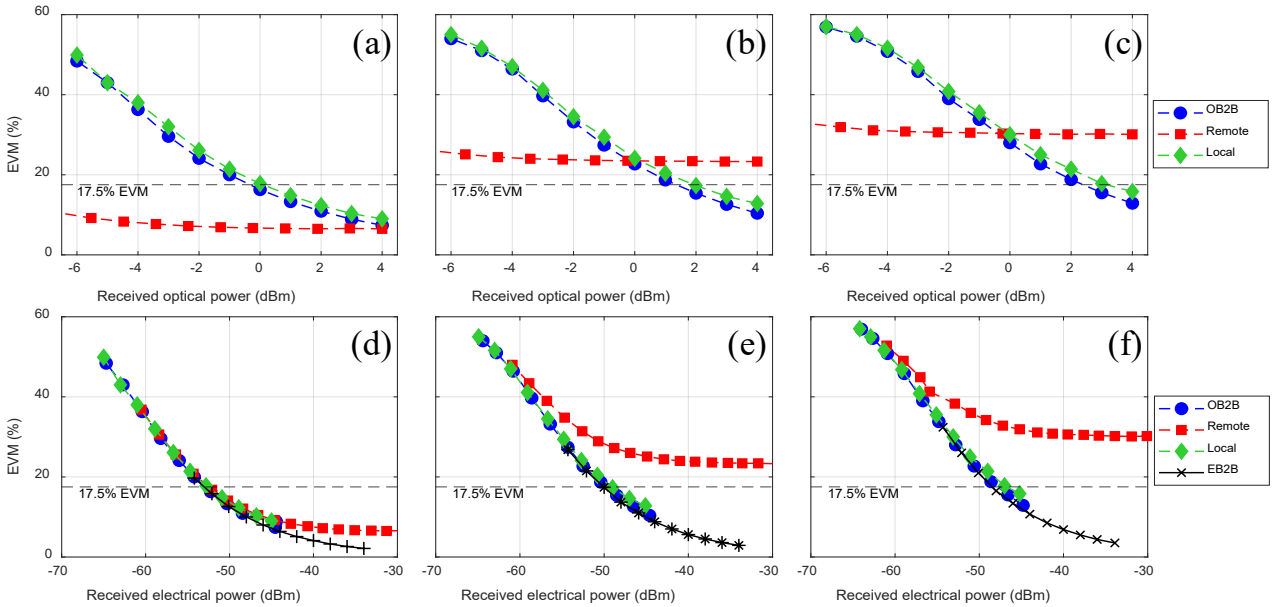

Fig. 10. EVM measurements of different QPSK signal bandwidth centered at 39.9 GHz (f_1 =100 MHz) vs RoP (top) and ReP (bottom): (a), (d) 50 MHz, (b), (e) 100 MHz and (c), (f) 150 MHz.

schemes, respectively. It can be observed that the carrier suppression is larger than 30 dB. Note the ASE noise level is 6 dB lower in remote setup due to higher optical power level at the EDFA input.

B. Electrical spectrum measurements

In this section, spectral measurements of recovered electrical signals after photodetection are shown in order to identify the nonlinear response of the optical fronthaul link under different signal transmission schemes.

B.1. Single-band transmission

The first experiment consists of transmitting a single band QPSK signal centered at 39.9 GHz (f_{RF} = 20 GHz, f_1 = 100 MHz) with variable bandwidth under OB2B, local and remote configurations. Fig. 6(a) and (b) shows the entire electrical spectra of 50 and 150 MHz bandwidth signal, respectively, transmitted under local configuration where the insets show the detail at baseband and mmW band. According to the HD frequency response shown in Table II and Fig. 2, 2ω-type harmonic distortions cannot be observed in the spectrum. However, Fig. 6(c) and (d) shows the spectra obtained when similar signals are transmitted under remote configuration. In this case, the detail at mmW band shows new frequency terms appeared as a result of system IMD, which is larger for signals with higher bandwidth (i.e. 150 MHz). Note that the electrical power is similar than measured in local setup for both signals at baseband whereas it is significantly different at mmW, where remote scheme leads to higher amplitude signal compared to the local configuration as a result of the combined effect of dispersion and laser chirp [11].

B.2. Dual-band transmission

In the following, two experiments are done with regards to transmit a two-band 50 MHz bandwidth signal, first centered at $f_1 = 100$ MHz and $f_2 = 200$ MHz and then, at $f_1 = 1$ GHz and $f_2 = 2$ GHz, respectively and the results were similar in both of them. Fig. 7(a) and (b) show electrical spectra obtained for the latter experiment under local and remote configurations, respectively. Corresponding insets show again the details of the spectra at baseband and mmW band. As expected, the local scheme leads to similar signal spectra in both bands whereas remote scheme causes several distortion frequency tones in the mmW band.

B.3. Three band transmission

Finally, a signal composed of three bands centered at 200, 325 and 525 MHz is transmitted over 40 GHz by using the local and remote schemes. As expected from the discussions above, the local configuration shows three bands without any other frequency component due to the absence of system nonlinearities (see Fig. 8(a)). However, the remote scheme leads to several frequency terms as shown in Fig. 8(b). Then, measurements were repeated under both transmission schemes by switching off the lower frequency bands (Fig. 8(c)) and (d) for local and remote setups, respectively). While the 525 MHz band remained unaffected in both schemes, note that, in this

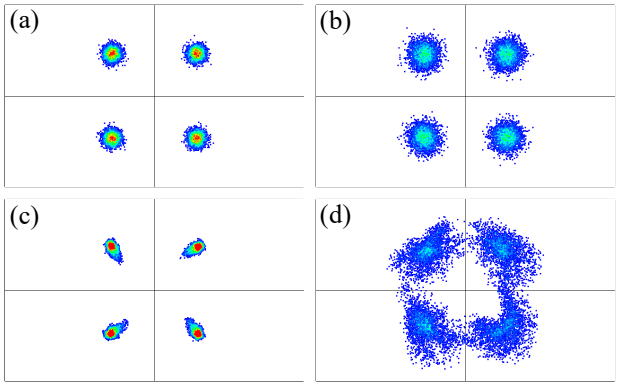

Fig. 11. In-band recovered QPSK signal constellations of f_1 = 100 MHz with RoP = 3 dBm at 39.9 GHz under local (top) and remote (bottom): (a), (c) 50 MHz; (b), (d) 150 MHz.

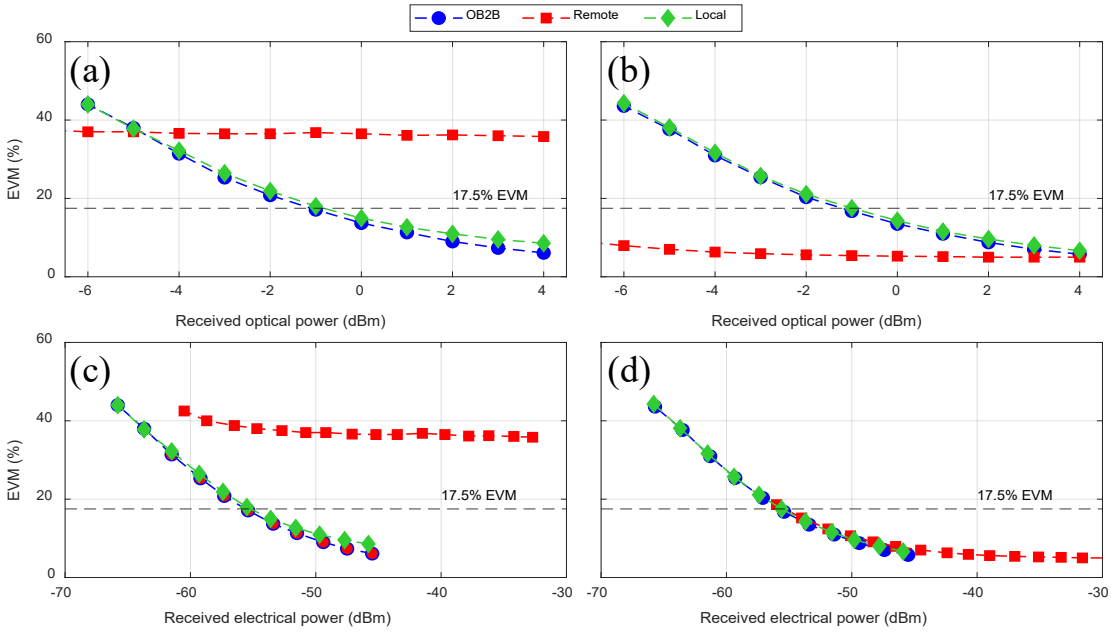

Fig. 12. OB2B, local and remote scheme measurements of EVM for evaluating out of band intermodulation at the frequency $2f_{RF}$-f_2 vs RoP (top) and ReP (bottom). Graphs (a) and (c) corresponds to a dual-band transmission (f_1= 1 GHz and f_2= 2 GHz) whereas graphs (b) and (d) are measured when f_2 is only transmitted.

case the nonlinear products created from the combination of different frequencies disappear since only one band is transmitted. Additionally, note that, unlike the spectra shown in Fig. 6(d) where HD was observed due to 150 MHz bandwidth signal centered at f_1 = 100 MHz, Fig. 8(d) shows the spectrum of a 50 MHz bandwidth signal at 525 MHz, and therefore, no HD can be observed due to (2ω)-type terms.

However, note that, as discussed above, due to the system frequency response, the power levels are higher under remote configuration in the mmW band (Fig. 8(a) and (b)) and some nonlinearities might be also due to power level. For the sake of verifying the reasons for them, Fig. 9(a), (b) and (c) show OB2B, local and remote measurements under the same power level conditions. In spite of the equal power level, the nonlinearities are clearly shown under remote configuration, as expected from the analytical formulation derived in Section II of the paper.

C. Transmission results

In this section, we evaluate the quality of recovered data after signal transmission under local and remote mmW signal generation schemes with special focus on the impact of system nonlinearities for different signals. Measurements have been done for different RoP values and also, in terms of the received electrical power (ReP) which corresponds to integrated electrical power of the mmW band provided by the vector signal analyser and was also adjusted by using the VOA.

C.1. Impact of (2ω$_1$)-type HD term

A single band QPSK signal (f_1 = 100 MHz) of variable bandwidth (50-150 MHz) is transmitted over $2f_{RF}$ = 40 GHz. Fig. 10(a) shows that remote configuration leads to better performance, i.e. lower EVM, than local and OB2B links, as expected from [11] over the whole received optical power (RoP) measurement range for 50 MHz bandwidth signal. However, broader signals with 100 and 150 MHz bandwidth show this behavior just up to a certain value of RoP, i.e. below 0 dBm in our setup (Fig. 10(b) and (c)). In these cases, remote configuration leads to EVM values which are independent from the RoP due to the impact of nonlinear response which prevents to show the EVM decrease with increasing RoP. Since this effect does not occur in local configuration (i.e. similar response to OB2B), a signal quality outperformance will be achieved under local scheme for RoP values above certain level. It is very interesting to show EVM measurements in terms of received electrical power (ReP) since the signal quality reflects the ReP actual value in all configurations and any deviation from the OB2B curve reports some degradation present in the system. Remote configuration leads to nonlinearities, as described in Section II, which are responsible of the increase of EVM values with respect to OB2B in Fig. 10(e)-(f) for ReP values larger than -62 dBm. Concretely, EVM values have suffered an 18 % and 22.5 % deterioration with -40 dBm ReP for signals bandwidth signals of 100 and 150 MHz, respectively, with regards to EB2B signal transmission.

Note that Figs. 10 (a)-(c) show a 10 dB RoP range which correspond to 20 dB ReP range so the results are equivalent in such range. Moreover, RoP curves lead to observe 15 dB difference between local and remote configurations, which is

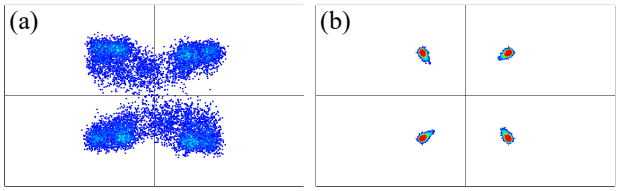

Fig. 13. QPSK signal constellations for the second band located at f_2 = 2 GHZ over remote scheme when (a) both bands and (b) only one are transmitted (-2.48 dBm RoP).

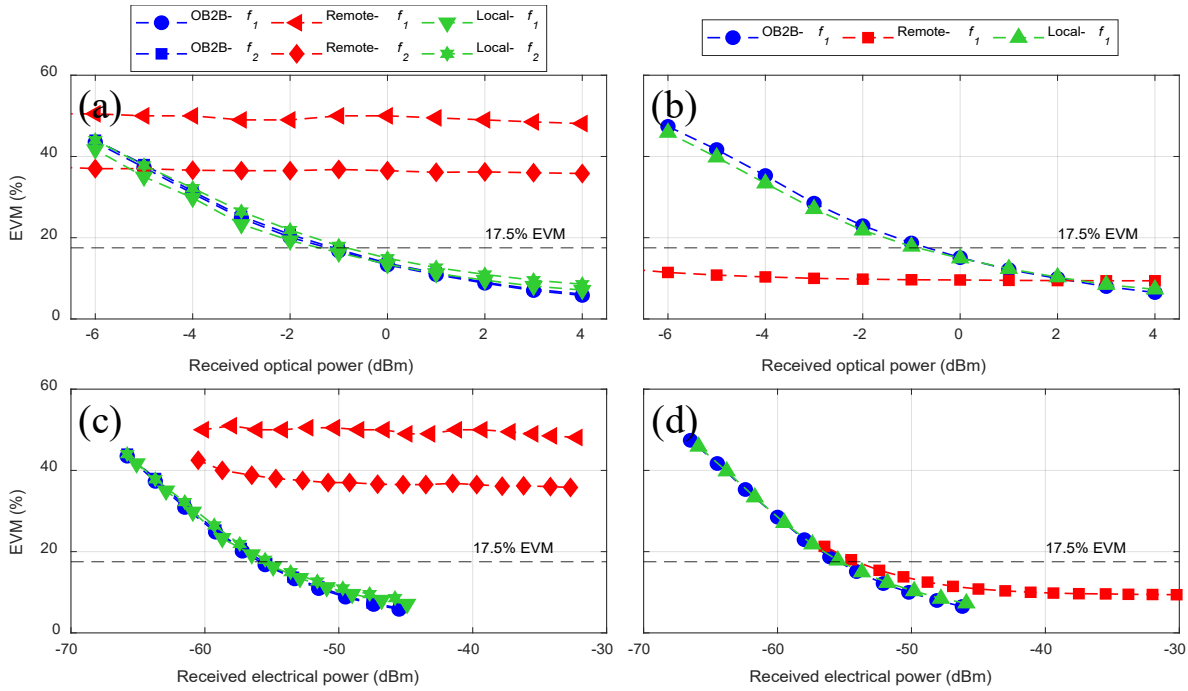

Fig. 14. OB2B, local and remote scheme measurements of EVM vs RoP (top) and ReP (bottom) carried by $2f_{RF}$-f_1: (a), (c) dual-band transmission (f_1 = 1 GHz and f_2 = 2 GHz); (b), (d) Only f_1 = 1 GHz is transmitted.

due to the intrinsic gain obtained in the remote configuration arisen from the combination of fiber dispersion and chirp [10].

Fig. 11 shows the measured constellations with 3 dBm RoP. While signal quality improvement is observed in remote setup compared to local on in 50 MHz bandwidth signal due to the aforementioned higher system response, clear impact of IMD in remote scheme is observed compared to local one in 150 MHz bandwidth QPSK signals and, accordingly to previous discussion. Additionally, measurements were repeated using a different value of central frequency (f_1 =200 MHz) with qualitative similar results, as expected from the previous sections.

Then, a 50 MHz bandwidth dual-band (f_1 =1 GHz and f_2 =2 GHz) QPSK data was transmitted to evaluate the EVM performance at $f_2 = 2f_1$ under B2B, local and remote configurations. In this case, we analyse the out of band nonlinearity due to the contribution ($2\omega_1$)-type HD, as calculated in Table II and measured in Fig. 2. Fig. 12 shows the EVM measurement vs RoP (top) and ReP (bottom) for B2B, local and remote configurations.

As shown in Fig. 12(a), measurements under remote mmW signal generation scheme lead to a high EVM constant value (38 %) over the measured RoP range due to second order HD penalty whereas local measurements of the second band are similar to OB2B.

This is confirmed in Fig. 12(b) when one band is switched off and those high EVM values are significantly reduced (below 10 %) due to the disappearance of ($2\omega_1$)-type HD contribution. When only one band is transmitted, this band in the remote scheme outperforms the local scheme due to the combined effect of laser chirp and fiber dispersion [11], as previously mentioned.

EVM measurements vs ReP allow to identify system degradations in addition to the frequency system response, so, as expected, OB2B and local scheme measurements are identical whereas remote scheme shows high EVM values over the threshold over the entire ReP measurement range due to IMD penalty, i.e. 38 % EVM at -40 dBm ReP. However, when f_1 band is switched off, EVM is reduced to 6 % due to the fact that this penalty mainly disappears, as depicted in Fig. 12(d).

Fig. 13(a) and (b) show the recovered signal constellations at f_2 over mmW band in remote scheme when both bands and only f_2 are transmitted for -2.48 dBm RoP. As can be observed, there is a strong signal distortion of the transmitted data due to second order HD in remote scheme in the former case and therefore, signal transmission cannot be held (Fig. 13(a)) while the signal quality is good (Fig.13(b)) when HD is suppressed.

C.2. Impact of ($\omega_2 - \omega_1$)-type IMD term

In order to evaluate the IMD term corresponding to ($\omega_2 - \omega_1$), we consider two RF subcarriers centered at the frequencies f_1 = 1 GHz and f_2 = 2 GHz with a 50 MHz-bandwidth QPSK data.

Fig. 14 shows the evaluation of the EVM performance of data carried by both frequencies under B2B, local and remote setups and also by the f_1 when only this one is transmitted. As shown in Fig. 14(a), measurements under remote mmW signal

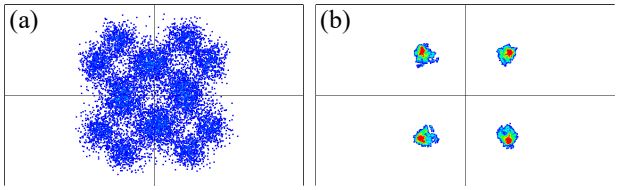

Fig. 15. QPSK signal constellations of f_1= 1 GHz over remote scheme when (a) f_1 and f_2 (b) only f_1 is transmitted (-2.48 dBm RoP).

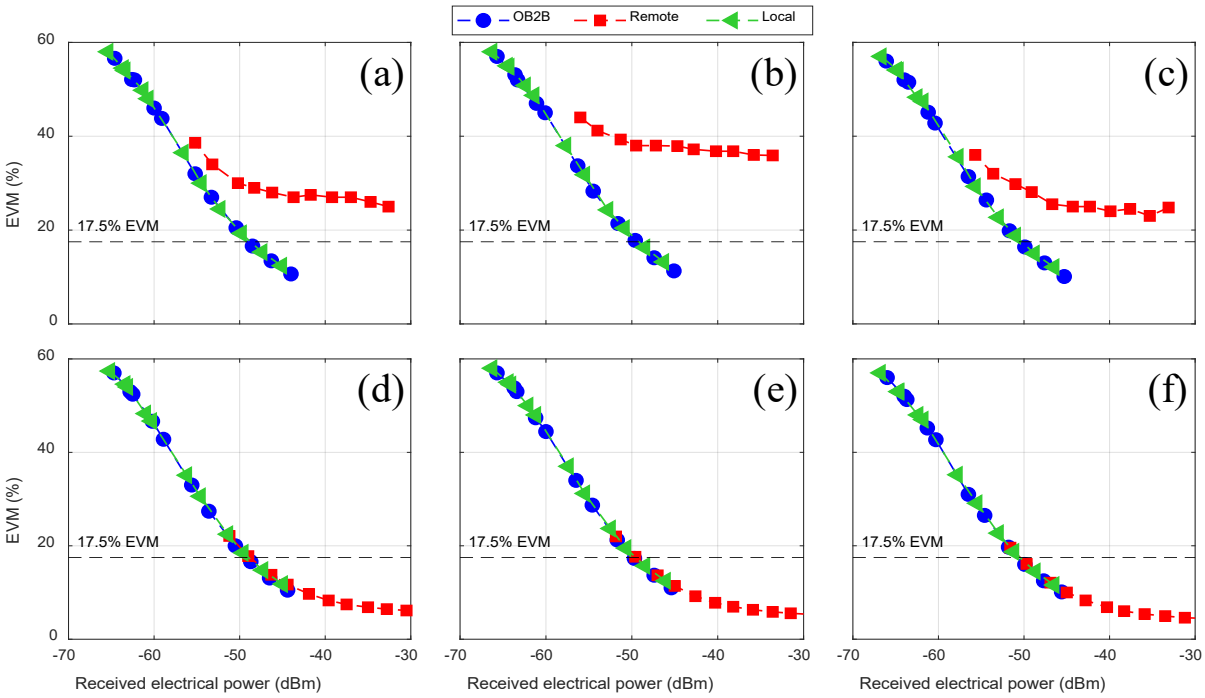

Fig. 16. EVM for OB2B, local and remote configurations of data carried by $2f_{RF}$-f_3 vs ReP when three bands are transmitted (top) and only f_3 is transmitted (bottom). Frequency bands are f_1 = 200 MHz, f_2 = 325 MHz and different f_3 as: (a), (d) f_3 = 400 MHz; (b), (e) f_3 = 525 MHz and (c), (f) f_3 = 650 MHz.

generation scheme lead to high EVM constant values over the measured RoP range due to IMD penalty whereas local measurements of the second band are similar to OB2B. Note that data carried over f_1= 1 GHz shows worse quality compared to carrier with f_2= 2 GHz (i.e. higher EVM), as expected from Figs. 2 and 3 since second order HD term affecting f_2 is lower than IMD term affecting f_1 , respectively.

Again, EVM measurements vs ReP are done to identify system degradations, and, as expected, OB2B and local scheme measurements are identical whereas remote scheme shows high EVM values over the threshold over the entire ReP measurement range (52 % for f_1 at -40 dBm ReP). Note that measured EVM values are different for both bands due to the reasons explained above. However, when the second band is switched off, $(\omega_2 - \omega_1)$-type IMD does not occur, EVM of f_1 signal drops to 12 % at -40 dBm ReP and only slight differences are measured due to the lack of perfect power adjustment in the experimental setup.

Fig. 15(a) and (b) show the recovered signal constellations at f_1=1 GHz over remote scheme when both bands and only one are transmitted for -2.48 dBm RoP, respectively. As can be observed, there is a strong signal distortion of the transmitted data due to IMD in remote scheme and therefore signal transmission cannot be held in the former case while the signal quality is good when IMD due to $(\omega_2 - \omega_1)$-term is cancelled.

C.2. Impact of $(\omega_2 + \omega_1)$-type IMD term

Finally, a three-band signal (f_1=200 MHz, f_2=325 MHz and f_3= 525) 50 MHz bandwidth QPSK data is transmitted over 40 GHz to evaluate the impact of $(\omega_2+\omega_1)$-type IMD term. Fig. 16 plots the EVM performance, which is studied in terms of ReP under OB2B, local and remote configurations of f_3 signal when the three bands are transmitted and when only the third one is transmitted. In this case, Fig. 16(a) and (c) corresponds with the EVM impact of $2\omega_1$ and $2\omega_3$, HD, respectively, whereas Fig. 16(b) corresponds to the $(\omega_2+\omega_1)$-type IMD term.

EVM vs ReP measurements again provide information of signal distortions independently on the frequency system response. Firstly, we observe that the EVM values for OB2B and local scenarios are similar for all RF carriers. Moreover, significant distortion under remote configuration is observed when three bands are transmitted showing similar values when $\omega_3 = 2\omega_1$ or $\omega_3 = 2\omega_2$ but higher in the second scenario with $\omega_3 = \omega_1 + \omega_2$.

As predicted in the theoretical analysis (Section II), the distortion level for low frequency (< 3.5 GHz) is similar for OB2B and local configuration and therefore, the EVM performance is very similar whereas measurements obtained under remote scheme show different behavior. Additionally, the EVM is approximately constant for ReP values larger

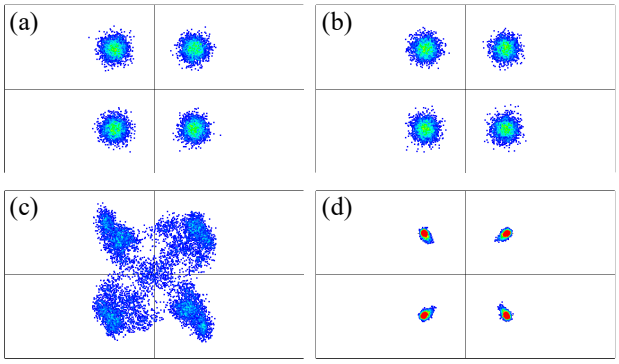

Fig. 17. Signal constellations of f_3 signal under local (a, b) and remote (c, d) schemes: (a), (c) three bands transmission and (b), (d) single band is transmitted.

than -50 dBm (38 %) (see Fig. 16(b)) which is higher than the EVM value of 29 % obtained in Fig. 16(a) and (c). As predicted in Section II, the distortion level difference is close to 10 dB for remote configuration comparing the amplitude response between Figs. 2 and 4. Therefore, it expected that the impact of second-order IMD is higher than HD contribution.

Finally, constellations under local and remote setup for the scenario with $\omega_3 = \omega_1 + \omega_2$ are shown in Fig. 17 to show the inability to transmit multiband signals due to IMD under remote configuration. In case of single band transmission, clear constellations with reduced EVM values are obtained in both setups (see Fig. 17(b) and (d)). On the contrary, multiband transmission does not lead to any significant impact under local configuration.

Although the experiments employed a signal composed of two bands, the results can be applied to Orthogonal Frequency Division Multiplexed (OFDM) signals typically employed in 5G/6G networks. Therefore, remote configuration can be employed for OFDM waveforms provided the different subcarriers fall apart from the HD and IMD frequency terms described above. Otherwise, local configuration will provide better performance due to the impact of nonlinear distortions. Furthermore, recently published advanced linearization techniques for reducing DML induced HD and IMD [19] can be employed in further work to improve the performance in both local and remote schemes, thus reinforcing the future deployment.

IV. Conclusions

This paper presents a comprehensive analytical derivation and experimental evaluation of the impact of harmonic and intermodulation distortion on data transmission over local and remote photonically generated mmW signals over an optical fiber fronthaul based on a DML and CS-external modulation for frequency up-conversion. Frequency response of the different second-order nonlinear terms, i.e. $(2\omega_1)$, $(\omega_2 - \omega_1)$ and $(\omega_1 + \omega_2)$, has been measured leading to -40 dBm, -30 dBm and -30 dBm, respectively, for a 40 GHz signal under remote configuration while local and OB2B setups lead to negligible IMD levels far from the relaxation frequency (< 6.5 GHz for the used DML). Measured electrical spectra show the effect of in-band IMD, as a function of the signal bandwidth, and out-of-band IMD in multiband signals.

EVM measurements of recovered QPSK signals show that transmission is not feasible under remote scheme for optical power levels above certain threshold while local scheme resembles OB2B transmission. As expected from theory [11], remote setup outperforms OB2B and local setup (e.g. 50 % compared to 10 % EVM at -6 dBm RoP using a 50 MHz bandwidth QPSK signal) up to certain RoP value. However, signal transmission is limited by $(2\omega_1)$-type HD and higher RoP values lead to poor signal transmission under remote compared to local setup. This effect is worse for larger bandwidth signals (i.e. from 12 % to 30 % EVM at 4 dBm RoP for 150 MHz bandwidth signal at 39.9 GHz). In two-band signals transmission $(\omega_2 = 2\omega_1)$, a 32 % EVM deterioration is measured with respect to singleband transmission at -40 dBm ReP.

Multiband signal transmission experiments have been also carried out to evaluate the effect of other second-order IMD terms. Concretely, the impact of $(\omega_2 - \omega_1)$type term, which is higher than $(2\omega_1)$-type term, and shows a 40 % deterioration at -40 dB ReP under remote configuration. However, the impact of $(\omega_1 + \omega_2)$-type term has been measured as lower, with a 29 % deterioration at -40 dBm ReP, in good agreement with the corresponding measured IMD frequency response.

Finally, the paper shows that, in spite of the better performance achieved under remote photonic mmW signal generation in C-RAN due to the combined effect of fiber dispersion and laser chirp, IMD terms prevent the transmission of specific signals under this setup. More concretely, wideband signals with in-band IMD or multiband signals (ω_1, ω_2, ω_3) satisfying $\omega_2 = 2\omega_1$, $\omega_1 = \omega_2 - \omega_1$ or $\omega_3 = \omega_1 - \omega_2$ are examples that need to be transmitted over local generation mmW approach in C-RAN. Therefore, the presented results provide valuable guidelines for 6G networks deployment in concrete application scenarios.

Acknowledgment

This work has been funded by the regional project Generalitat Valenciana (PROMETEO 2021/015) and Grant RTI2018-101658-B-I00 FOCAL by MCIN/AEI/ 10.13039/501100011033 and ERDF “A way of making Europe”.

References

[1] R. I.-R. M.2370-0, “IMT Traffic Estimates for the Years 2020 to 2030,” 2015.

[2] W. Jiang, B. Han, M. A. Habibi and H. D. Schotten, “The Road Towards 6G: A Comprehensive Survey,” *IEEE Open J. Commun. Soc.*, vol. 2, pp. 334-366, 2021.

[3] R. Waterhouse and D. Novack, “Realizing 5G: Microwave Photonics for 5G Mobile Wireless Systems,” *IEEE Microw. Mag.*, vol. 16, no. 8, pp. 84-92, 2015.

[4] C. Lim and A. Nirmalathas, “Radio-Over-Fiber Technology: Present and Future,” *J. Lightw. Technol.*, vol. 39, no. 4, pp. 881-889, 2021.

[5] C. Lim, Y. Tian, C. Ranaweera, T. A. Nirmalathas, E. Wong and K.-L. Lee, “Evolution of radio-over-fiber technology,” *J. Lightw. Technol.*, vol. 37, no. 6, pp. 1647-1656, 2019.

[6] C. Ranaweera, E. Wong, A. Nirmalathas, C. Jayasundara and C. Lim, “5G C-RAN with optical fronthaul: an analysis from a deployment perspective,” *J. Lightw. Technol.*, vol. 36, no. 11, pp. 2059-2068, 2018.

[7] C. Liu, J. Wang, L. Cheng, M. Zhu and G.-K. Chang, “Key microwave-photonics technologies for next-generation cloud-based radio access networks,” *J. Lightw. Technol.*, vol. 20, no. 3452-3460, p. 32, 2015.

[8] J. Yao, “Microwave Photonics,” *J. Lightw. Technol.*, vol. 27, no. 3, pp. 314-335, 2009.

[9] S.-P. Dai, C.-T. Lin, S. Chi, P.-C. Peng and J. Chen, “Impact of nonlinear transfer function and imperfect splitting ratio of MZM on optical up-conversion employing double sideband with carrier suppression modulation,” *J. Lightw. Technol.*, vol. 15, no. 2449-2459, p. 26, 2008.

[10] J. Ma, J. Yu, C. Yu, X. Xin, J. Zeng and L. Chen, "Fiber Dispersion Influence on Transmission of the Optical Millimeter-Waves Generated Using LN-MZM Intensity Modulation," *J. Lightw. Technol.*, vol. 25, no. 11, pp. 3244-3256, 2007.

[11] L. Vallejo, J. Mora, D.-N. Nguyen, J. Bohata, V. Almenar, S. Zvanovec and B. Ortega, “On the 40 GHz Remote versus Local Photonic Generation for DML-based C-RAN Optical Fronthau,” *J. Lightw. Technol.*, vol. 39, no. 21, pp. 6712-6723, 2021.

[12] C. Lim, A. Nirmalathas, K.-L. Lee, D. Novak and R. Waterhouse, “Intermodulation Distortion Improvement for Fiber–Radio Applications Incorporating OSSB+C Modulation in an Optical Integrated-Access Environment,” *J. Lightw. Technol.*, vol. 25, no. 6, pp. 1602-1612, 2007.

[13] J. Wang, C. Liu, M. Zhu, A. Yi and G.-K. Chang, "Closed-form analysis of intra/inter-band cross-modulation in multiband radio-over-fiber systems," in *2013 IEEE Glob. Commun. Conf. (GLOBECOM)*, 2013.
[14] K. Kojucharow, M. Sauer and C. Schaffer, "Millimeter-wave signal properties resulting from electrooptical upconversion," *IEEE Trans. Microw. Theory Tech.*, vol. 49, no. 10, pp. 1977-1985, 2001.
[15] L. A. Neto, E. Didier, G. Naveena, C. Philippe, D. Qian, T. Fatoumata, A. Thomas, H. Rajaâ and A.-B. Christelle, "Simple estimation of fiber dispresion and laser chirp parameters using the downhill simplex fitting algorithm," *J. Lightw. Technol.*, vol. 31, no. 2, pp. 334 - 342, 2013.
[16] J. Le Bihan and G. Yabre, "FM and IM intermodulation distortions in directly modulated single-mode semiconductor lasers," *IEEE J. Quantum Electron.*, vol. 30, no. 4, pp. 89-904, 1994.
[17] L. Zhang and D. A. Ackerman, "Second- and third-order harmonic distortion in DFB lasers," *IEEE J. Quantum Electron.*, vol. 31, no. 11, pp. 1974-1980, 1995.
[18] I. P. Kaminow, T. Li and A. E. Willner, Optical Fiber Telecommunications Volume VIB: Systems and Networks, Academic Press, 2013.
[19] N. Bamiedakis, D. G. Cunningham and R. V. Penty, "Linearisation Method of DML-based Transmitters for Optical Communications Part II: Experimental Demonstration and Implementation Methods," *J. Lightw. Technol.*, vol. 39, no. 18, pp. 5828-5836, 2021.

Luis Vallejo (Member, IEEE) was born in Malaga, Andalucia, Spain, in 1991. He received the B.Sc. degree in Telecommunication Technology Engineering in 2016 and the M.Sc in Telecommunication Engineering in 2017 from the Universidad de Malaga, Spain. He did a Test and Verification Engineer Internship at Keysight Technologies in 2017. He joined Instituto de Telecomunicaciones y Aplicaciones Multimedia (iTEAM), Photonic Research Labs (PRL), at the Universitat Politecnica de Valencia (UPV), Spain, in 2018. He is currently pursuing the PhD degree in Telecommunication Engineering program in UPV. His research interests include microwave photonics, mmW generation, RoF/FSO for 5G and beyond, and optical access networks.

José Mora was born in Torrent, Valencia, Spain, in 1976. He received the M.Sc. degree in Physical Sciences from the Universitat de València (Spain) in 1999. From 1999 to 2004, he worked in the Department on Applied Physics from the Universitat de València. He holds on a PhD. Degree in Physics from the Universitat de València in 2005 and he received the Extraordinary Doctorate Prize of the Universitat de València in 2006. Since 2004, he joined as a researcher at the Optical and Quantum Communications Group in the Institute of Telecomunications and Multimedia (ITEAM) from the Universitat Politècnica de València. He has been involved in the EU funded projects IST-LABELS, IST-GLAMOROUS, IST-OFFSOHO, IST-NEFERTITI and ICT-ALPHA. With an H-factor of 15, he has published more than 100 papers and conference contributions covering a wide range of fields related to fibre bragg gratings for sensing applications, optical signal processing, microwave photonics, reconfigurable and convergent optical for wired/wireless services and quantum cryptography using photonic technology.

Beatriz Ortega (Senior Member, IEEE) received the M.Sc. degree in Physics in 1995 from the Universidad de Valencia, and the Ph.D. in Telecommunications Engineering in 1999 from the Universidad Politécnica de Valencia. She currently works at the Departamento de Comunicaciones from the Universitat Politècnica de València, where she holds a Full Professorship since 2009 and collaborates as a group leader in the Photonics Research Labs in the Institute of Telecommunications and Multimedia Applications. She has published more than 200 papers and conference contributions in fibre Bragg gratings, microwave photonics and optical networks. She has got several patents and is also a co-founder of EPHOOX company. She has participated in a large number of European Networks of Excellence and R&D projects and other national ones. Her main research is currently focused on optical devices, optical networks and microwave photonic systems and applications.